

NUMERICAL STUDY ON THE MIXING CHARACTERISTICS UNDER TRANSCRITICAL AND SUPERCRITICAL INJECTION USING LARGE EDDY SIMULATION

by

**Wu WEI^{a*}, Wenzhi DONG^a, Wenjin QIN^b, Meng YUE^c,
and Maozhao XIE^c**

^a School of Mechanical Engineering, Guizhou University, Guiyang, China

^b School of Mechanical Engineering, University of Shanghai for Science and Technology,
Shanghai, China

^c School of Energy and Power Engineering, Dalian University of Technology,
Dalian, China

Original scientific paper

<https://doi.org/10.2298/TSCI200625136W>

Large eddy simulations of cryogenic nitrogen injection are performed on both transcritical and supercritical injection and mainly attentions are focus on the jet disintegration mechanism and mixing layer feature. The simulation results reveal that the thermal disintegration mechanical dominates the disintegration characteristic under supercritical conditions. The jet disintegration is delayed and longer dense core region is detected for the transcritical injection due to the large density gradient effects. Because of this disintegration mechanism, the Reynolds stresses in the transcritical case are significantly suppressed in the turbulent fluctuation. In addition, we define a mixing layer based on the density gradient and thicker mixing layer interfaces are formed in the supercritical case. The relationship between transport properties and the large density gradient are also investigated, results indicate that the large density gradients are influenced by the pseudo critical temperature and transport properties.

Key words: *large eddy simulations, jet disintegration, mixing layer, thermodynamic and transport properties*

Introduction

Recently, energy security and environmental pollution have posed a great challenge to the automotive industry. To improve combustion efficiency and reduce pollutant emissions, the pressure in the chamber is higher than the critical pressure, P_c , of the injected fuel in cryogenic rocket engines or internal combustion engines. In such conditions, the injection behavior may strongly differ from that in sub-critical injection, and was not well understood in recent years.

For the purpose of understanding the breakup and mixing characteristic under supercritical condition, both research institutions Air Force Research Laboratory and German Aerospace Center have done extensive experimental studies with cryogenic nitrogen injected into supercritical gas nitrogen environment [1-4]. Results in these experiments showed a striking different disintegration between the supercritical and subcritical injection. It is not broken into

* Corresponding author, e-mail: weiwu811@163.com

droplets as it happened during sub-critical injection, finger-like structures emerged from the jet core, which is located in areas far from the injector. In addition, Davis *et al.* [5] studied the influence of acoustic perturbations on both supercritical and subcritical injection regimes, and demonstrated that the supercritical injection regime is more easily affected by the acoustic perturbations than that in sub-critical pressure jets.

Along with these experimental investigations, the numerical simulation is a powerful tool to analyze and study the extreme phenomena of supercritical injection. Researcher in [6-8] performed a simulation on the heptane-nitrogen mixing layer using direct numerical simulation. They found that the density-gradient play an important role on supercritical mixing behavior, hence a special model should be developed for such high pressure injection. Selle and Schmitt [9] devoted to investigating the effects of real gas equation of state on turbulence properties and turbulence models. They showed that the spectral content of flow is not affected by the peculiar thermodynamic properties. Yang and Vigor [10] and Zong *et al.* [11] performed simulations on cryogenic nitrogen injection at different pressure conditions, and they suggested that the density gradient has the effects of stabilizing the jet evolution. Park [12] studied the influence of turbulence model on supercritical jet and found that the turbulence models have limited effects on supercritical injection and subcritical models can be applied to supercritical condition. Recently, Simeoni *et al.* [13] and Banuti *et al.* [14] have demonstrated that supercritical fluid states are not homogeneously distributed, but can be divided into two different regions: gas-like and liquid-like behavior, which is analogous to the situation at subcritical conditions. These regions are separated by a so-called Widom line. Banuti and Hannemann [15] studied the thermal breakup mechanism under supercritical condition. They showed that thermal disintegration may dominate classical mechanical breakup when the fluid temperature close to the pseudo-boiling point. More extensive numerical investigations of the state of knowledge on supercritical mixing and combustion are available in literature [16-22].

Fang *et al.* [23] studied the effects of temperature on nanojet ejection process by molecular dynamics simulation. They showed that the atoms from the nanojet aperture are more evenly distributed as the temperature increase. This suggested that the injected temperature is crucial to the breakup characteristics. In micro regimes, Banuti and Hannemann [15] put forward the thermal disintegration mechanical for the breakup characteristic when the fluid transit across the pseudo-boiling point. However, this mechanism is only suitable to the transcritical injection, and the supercritical regimes have not been involved. Hence, in the present study, we focus on investigating on the disintegration mechanism for both transcritical and supercritical injection. Although there are many investigations on supercritical injection, the interface information seldom attracted attention in previous research. Hence, the mixing interface characteristic under supercritical condition is also investigated in this study.

Governing equations and equation of states

According to previous research, the Navier-Stokes (N-S) equations of low pressure flows are extended to the supercritical condition. By applying a Favre average to the equations of mass, momentum, and energy, and then the large eddy simulations (LES) equations for single-species are obtained:

$$\frac{\partial \bar{\rho}}{\partial t} + \frac{\partial (\bar{\rho} \tilde{u}_i)}{\partial x_i} = 0 \quad (1)$$

$$\frac{\partial(\overline{\rho\tilde{u}_i})}{\partial t} + \frac{\partial(\overline{\rho\tilde{u}_i\tilde{u}_j} + \overline{p\delta_{ij}})}{\partial x_j} = \frac{\partial(\tilde{\tau}_{ij} - \tau_i^{\text{SGS}})}{\partial x_j} \quad (2)$$

$$\frac{\partial\overline{\rho\tilde{e}_t}}{\partial t} + \frac{\partial[(\overline{\rho\tilde{e}_t} + \overline{p})\tilde{u}_i]}{\partial x_i} = \frac{\partial(\tilde{u}_j\tilde{\tau}_{ij} + \tilde{q}_i - H_i^{\text{SGS}} + \sigma_i^{\text{SGS}})}{\partial x_i} \quad (3)$$

where ρ , u_i , p , e_t , and τ_{ij} , denote the density, velocity, pressure, total energy, and shear stress, respectively. The overbars denote resolved-scale, and the tildes is Favre-averaged resolved-scale variables. The unclosed term including the stresses τ_{ij}^{SGS} , energy fluxes H_i^{SGS} , and viscous work σ_{ij}^{SGS} , are defined:

$$\tau_{ij}^{\text{SGS}} = (\overline{\rho u_i u_j} - \overline{\rho\tilde{u}_i\tilde{u}_j}) \quad (4)$$

$$H_i^{\text{SGS}} = (\overline{\rho e_t u_i} - \overline{\rho\tilde{e}_t\tilde{u}_i}) + (\overline{p u_i} - \overline{p\tilde{u}_i}) \quad (5)$$

$$\sigma_{ij}^{\text{SGS}} = (\overline{u_j \tau_{ij}} - \tilde{u}_j \tilde{\tau}_{ij}) \quad (6)$$

These SGS terms are difficult to obtain and models are needed. According to Park investigation [12], comparing to the equation of state, the sub-grid models had limited effects on supercritical injection. For simplicity, the Smagorinsky model [24] is applied in this study, and the stress term is defined:

$$\tau_{ij}^{\text{SGS}} = -2\nu_t \overline{\rho} \left(\tilde{S}_{ij} - \tilde{S}_{kk} \frac{\delta_{ij}}{3} \right) + \frac{2}{3} \overline{\rho} k^{\text{SGS}} \delta_{ij} \quad (7)$$

where

$$\nu_t = C_R \Delta^2 (2\tilde{S}_{ij}\tilde{S}_{ij})^{1/2}, \quad k^{\text{SGS}} = C_I \Delta^2 (2\tilde{S}_{ij}\tilde{S}_{ij})$$

$$H_i^{\text{SGS}} = -\overline{\rho} \frac{-\nu_t}{\text{Pr}_t} \left(\frac{\partial \tilde{h}}{\partial x_j} + \tilde{u}_i \frac{\partial \tilde{u}_i}{\partial x_j} + \frac{1}{2} \frac{\partial k^{\text{SGS}}}{\partial x_j} \right) \quad (8)$$

where C_R and C_I are dimensionless constants, they are determined empirically and equal to 0.01 and 0.007, respectively. The strain-rate tensor $\tilde{S}_{ij} = (\partial\tilde{u}_i/\partial x_j + \partial\tilde{u}_j/\partial x_i)/2$ and the symbol Δ represents the filter width: $\Delta = (\delta x \delta y \delta z)^{1/3}$, where δx , δy , and δz denote the three spatial dimensions. The $\text{Pr}_t = 0.7$ is the turbulent Prandtl number. In addition, the unclosed sub-grid viscous-work term σ_{ij}^{SGS} is small and difficult to determine, hence, it is neglected in this study.

Finally, an equation of state is needed to close the governing, previously given equations. Under supercritical conditions, the chosen of equation of state is crucial on the jet mixing feature and a real-gas equation is needed. For real-gas equation of state, the 32-term Benedict-Webb-Robin [25] can predict high accuracy for all PVT ranges. However, comparing to the cubic equation of state, e.g. PR [26] and SRK [27, 28] equation of state, the BWR equation is rather complex and high computational expense. Hence, the SRK equation of state is applied for it is sufficiently accurate at both transcritical and supercritical conditions. The thermodynamic properties, such as the specific enthalpy and internal energy and are calculat-

ed based on the real-gas equation of state, and the detailed derivation process is available in Kim *et al.* [29]. The transport properties including the viscosity and thermal conductivity are predicted by the model of Zeberg-Mikkelsen and Stenby [30] and Vasserman and Nedostup [31], respectively. By using the SRK and ideal gas EOS, the density, constant-pressure specific heat, thermal conductivity and viscosity are plotted and shown in fig. 1. Also, the NIST measurement data are given for comparison. As can be seen from the figure, in all temperature ranges the SRK EOS can predict the thermodynamics and transport properties well and agree well with the NIST data [32] except that there are some discrepancies around the pseudo critical temperature regions. However, the ideal gas EOS greatly underestimates the values. Therefore, the SRK equation of state is reliable for the prediction of thermodynamic and transport properties and will be used in the present study.

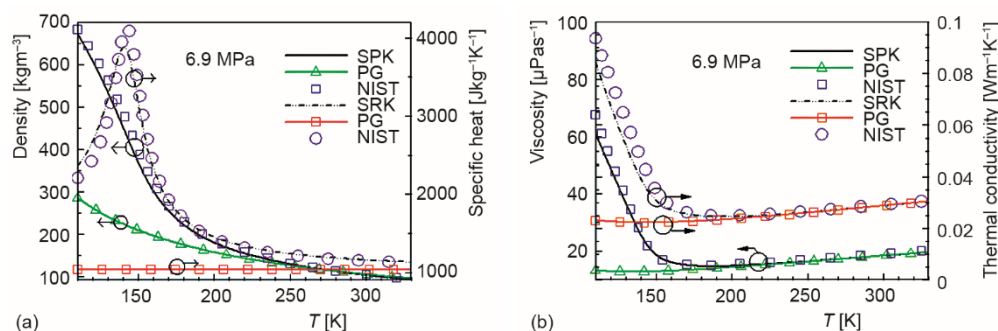


Figure 1. Comparison of the density, specific heat, viscosity, and thermal conductivity distribution based on different equation of state

Numerical method and flow configuration

Under supercritical conditions, the numerical simulation is a challenge task due to the high density ratio, thermodynamic non-idealities, and transport anomalies. The N-S equations are solved by finite-volume methodology and the centered scheme is applied. Both the convective and viscous terms are approximated using a second-order central scheme, along with a second-order implicit scheme for temporal derivatives. According to the method suggested by Park [12, 33, 34], the PISO algorithm is slightly modified to be capable of handling the real-gas fluid. To improve computation time, a multi-block domain decomposition technique with message passing interface is used for parallel computing.

Cryogenic nitrogen injected into a supercritical gas nitrogen environment is simulated with the model of experimental study from Cheroudi *et al* [30]. Initially, cold nitrogen is injected into a cylindrical chamber that is filled with warm nitrogen ($T_{\infty} = 300$ K) at a constant pressure of 6.9 MPa. The injector diameter is 0.254 mm, and the jet bulk velocity is sustained at 15 m/s. In addition, the velocity is imposed at the inlet with a fluctuating vorticity field prescribed by Mathey *et al.* [35], and an fluctuation intensity of 5.0% of the mean flow is imposed. The injected temperature is 120 K and 150 K, which is corresponding to transcritical and supercritical injection. The simulation conditions are shown in tab. 1, where the subscripts ∞ and inj denote the environment and injection conditions, respectively. The cylindrical computational domain is $40 D_{\text{inj}}$ in the axial directions with a diameter of $14 D_{\text{inj}}$, which is sufficient to characterize the mixing process. The 3-D domain is discretized by a grid system of $250 \times 100 \times 80$ in x , y , and z -directions, respectively.

Table 1. Physical parameters for simulation

Case	T_{inj} [K]	u_{inj} [ms^{-1}]	T [K]	p [atm]	ρ_{inj}/ρ_{∞}	Re_{inj}
1	120	15	300	69	7.8	44700
2	150	15	300	69	3.7	42300

Results and discussions

Instantaneous flow

Figure 2 shows the contour plot of density for the transcritical injection, and the graph of visual characteristics obtained by Riemann scattering technique in Chehroudi *et al.* [2] is also plotted for comparison. It is obvious that vortexes begin to grow up and finger-like structures begin to split out from the jet surface as the jet develops downstream. In addition, dense fluid pockets move far downstream, which is usually visualized in previous experimental investigation. Comparing the density contour plot with the experimental study, it is found that density contour is qualitatively consistent with experiment, indicating that LES is an efficient tool to reconstruct the flow field.

Figure 3 plots iso-surface of the density at $\rho_{1/2} = (\rho_{inj} + \rho_{\infty})/2$. In both cases, coherent structures begin to grow up outside the jet surface, leading to break-up of jet and dissolve into the surrounding environment. Through close observation, it is observed that the vortexes grow up earlier in the supercritical case due to the smaller density ratio between the injected fluid and surrounding gas. As a result, the transcritical Case 1 shows a much longer dense core.

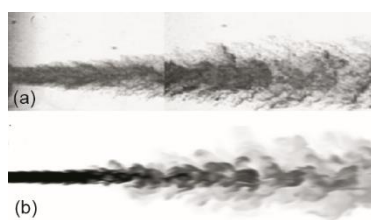


Figure 2. Shadowgraphs from Chehroudi [2] (a) and numerical shadowgraphs of density (b) in the axis plane

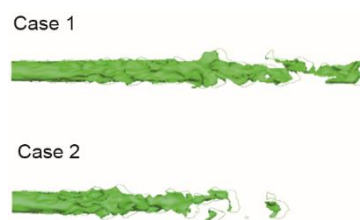


Figure 3. Comparison of instantaneous density iso-surface

Figure 4 shows the snapshots of density gradient, temperature, viscosity and thermal conductivity for both cases. It is observed that before $x/D_{inj} < 8$, the jet surfaces are surrounded by large density gradients, and the values are much larger in the transcritical case due to the large density ratio effects, which suppress radial velocity fluctuations and stronger density gradients are formed. Therefore, the cryogenic fluid jet in Case 1 moves deep downstream, forming a longer potential core region. To further understand the relation between the large density gradient and pseudo critical temperature, the dash line corresponding to the pseudo boiling temperature is also shown in the figure. It can be found that the dash line mainly transit across the largest density gradient region, indicating that the pseudo boiling temperature has the effects of forming large density gradient.

Under subcritical pressure condition, the constant pressure specific heat diverges at the boiling temperature, where heat is added during vaporization without increasing the tem-

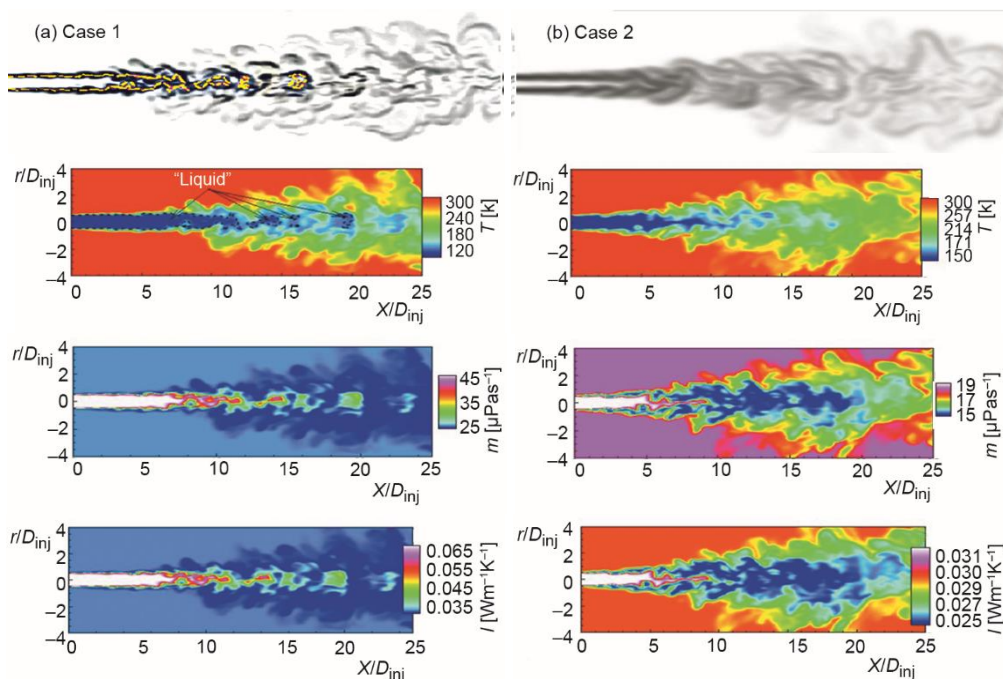


Figure 4. Snapshots of density gradient, temperature, viscosity, and thermal conductivity for Case 1 (a) and Case 2 (b); the dash lines represent the pseudo critical temperature (for color image see journal web site)

perature until all liquid is consumed. This behavior remains visible in supercritical pressures, while flatten and move to higher temperature with the increase of pressure [32]. As a result, analogous to the subcritical regime, we divide the supercritical regime into two parts: *liquid* regions before the temperature reach the pseudo boiling temperature and gas-like region where the temperature exceed its pseudo critical temperature. According to this definition, *liquid* block can be seen in the transcritical Case 1, which is marked by the dash line in the temperature distribution in fig. 4, while this phenomenon does not occur in the supercritical of Case 2. By careful observation, the *liquid* block move deep downstream, which is consistent with the shadowgraphs observed in experimental study in fig. 2.

The contour plots of viscosity and thermal conductivity are also plotted in fig. 4. For both cases, the viscosity and thermal conductivity show a similar distribution with a maximum value in the potential core region, and then decline as the jet mixes with the ambient gas, with a maximum value around the jet outside. By comparing the two injections, both the viscosity and thermal conductivity show a much larger values in the transcritical case, which is close to the liquid nitrogen properties. In order to quantitative understand the thermodynamic and transport properties in large density regions, the conditional averages of constant pressure specific heat, thermal conductivity and viscosity over regions where $|\nabla\rho| > \text{cutoff}$ for the two cases are listed in tabs. 2 and 3, respectively. In both case, the constant pressure specific heat increase as the cutoff value elevate, indicating that the large specific heat has the effects of forming large density gradient. The transport properties including the thermal conductivity and viscosity show the same trend as that of specific heat. Hence, large transport properties are easily formed in the large density gradient, which is consistent with the above contour plots.

Table 2. Conditional averages of constant pressure specific heat, diffusion coefficient, and viscosity over regions where $|\nabla\rho| > \text{cutoff}$ in Case 1

Cutoff	average C_p [Jkg ⁻¹ K ⁻¹]	average λ [Wm ⁻¹ K ⁻¹]	average μ [kgm ⁻¹ s ⁻¹]
0.1 $ \nabla\rho _{\text{max}}$	2.733e · 10 ³	3.79e · 10 ⁻²	2.499e · 10 ⁻⁵
0.2 $ \nabla\rho _{\text{max}}$	2.853e · 10 ³	4.12e · 10 ⁻²	2.772e · 10 ⁻⁵
0.3 $ \nabla\rho _{\text{max}}$	2.868e · 10 ³	4.20e · 10 ⁻²	2.837e · 10 ⁻⁵

Table 3. Conditional averages constant pressure specific heat, diffusion coefficient, and viscosity over regions where $|\nabla\rho| > \text{cutoff}$ in Case 2

Cutoff	average C_p [Jkg ⁻¹ K ⁻¹]	average λ [Wm ⁻¹ K ⁻¹]	average μ [kgm ⁻¹ s ⁻¹]
0.1 $ \nabla\rho _{\text{max}}$	1.922e · 10 ³	2.67e · 10 ⁻⁶	1.620e · 10 ⁻⁵
0.2 $ \nabla\rho _{\text{max}}$	2.104e · 10 ³	2.72e · 10 ⁻⁶	1644e · 10 ⁻⁵
0.3 $ \nabla\rho _{\text{max}}$	2.169e · 10 ³	2.75e · 10 ⁻⁷	1.647e · 10 ⁻⁵

Statistics average over flow properties

The instantaneous flow fields show that there are great different between the transcritical and supercritical injection, indicating that the disintegration mechanism is crucial to both the transcritical and supercritical injection. To further understand the disintegration mechanism, mean and statistically-steady quantities are calculated by taking a time average of the instantaneous flow data as the flow has reached its stationary state.

Figure 5 shows the radial distribution of normalized mean density at $x/D_{\text{inj}} = 20$ and 24 for both cases, where the density is normalized as: $\rho^* = (\bar{\rho} - \bar{\rho}_\infty) / (\bar{\rho}_c - \bar{\rho}_\infty)$ the $\bar{\rho}_c$ and $\bar{\rho}_\infty$ denote the mean density at the center and in the environment, respectively. The radial co-ordinate is normalized by the FWHM, which is defined as the radius at which the density is one half of its maximum value of the corresponding axial position. It can be found that the density before $r/r_{1/2}$ shows similar distribution, while the fluid move farther in the radial, especially at $x/D_{\text{inj}} = 24$, where the density distribution drop faster for the supercritical case. This is because the injected temperature in the supercritical case is above the pseudo-critical temperature corresponding to lower density ratio, leading to a faster disintegration of the jet. In addition, the experimental data obtained by Chehroudi [2] using the Raman scattering technique is also plotted for the transcritical case. The simulated density profiles in this study

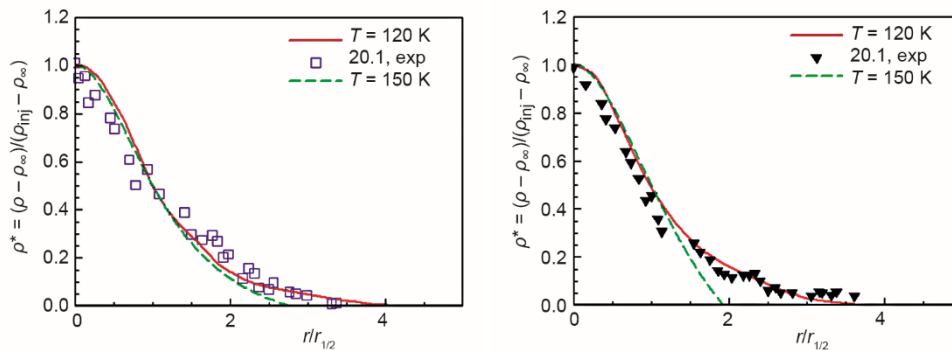


Figure 5. Radial distribution of normalized density at different axial locations

follow the trend well and agree well with the experiment, indicating that the numerical simulation is an effective tool for predicting the supercritical injection mixing process.

Figure 6 shows the radial distribution of the normalized velocity, constant-pressure specific heat and viscosity distribution at $x/D_{inj} = 5$ and 12. For the velocity distribution, a flat-hat distribution is visible near the injector at $x/D_{inj} = 5$. In the potential core region, the velocity in the supercritical case shows a little higher than the transcritical case after $r/D_{inj} = 0.6$. As the jet move downstream far from the inlet at $x/D_{inj} = 12$, the velocity around the axis drop fast in the supercritical case, while shows much greater value after $r/D_{inj} = 0.6$. This phenomenon is attributed to the density stratification effect, which is much stronger in the transcritical case. The high density stratification transfers turbulence kinetic energy from radial to axial direction. A spike exists in the specific heat profile at $r/D_{inj} = 0.5$ for the transcritical case at $x/D_{inj} = 5$, which is caused by the temperature transit across the pseudo-critical temperature. However, in the supercritical Case 2, the initial temperature is above the pseudo critical temperature, so that the specific heat decreases smoothly without a peak region. Similar profiles can be found at $x/D_{inj} = 12$, while the spike tends to move to the axis direction and the value slightly decrease. Interestingly, around the spike of specific heat profile, a minimum value is visible for the radial viscosity distribution. This phenomenon indicates that the thermodynamic properties play an important role on the supercritical evolution.

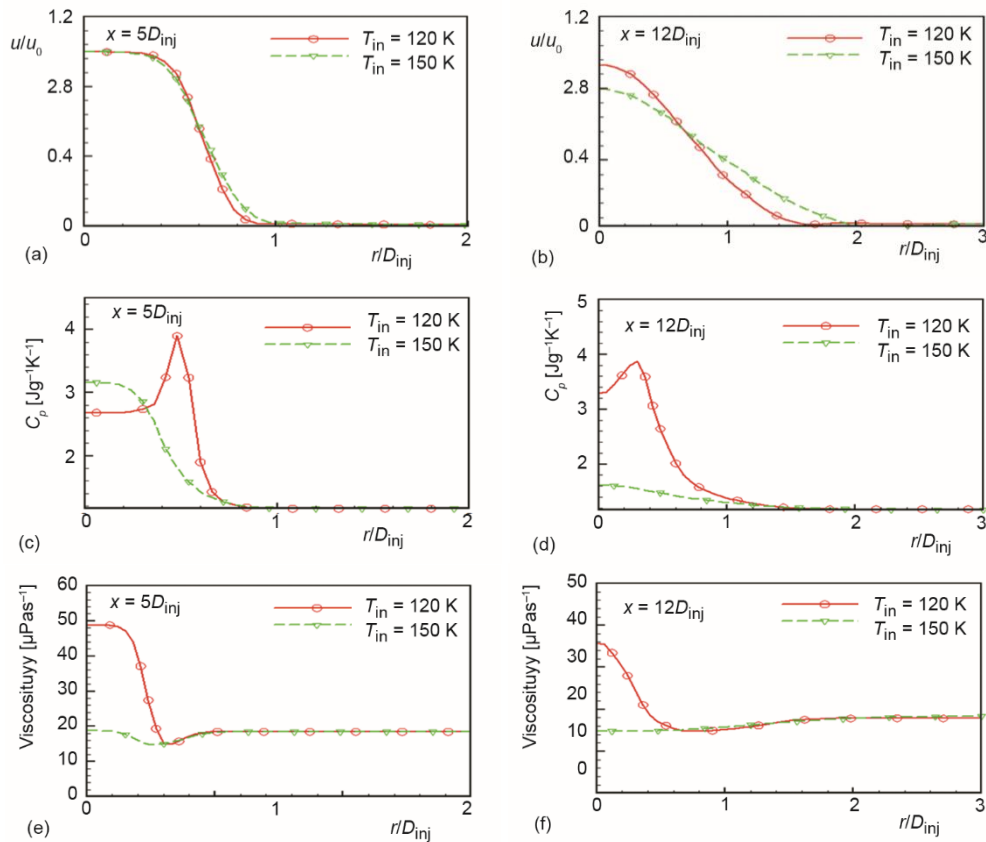


Figure 6. The velocity, constant-pressure specific heat, and viscosity distribution at $x/D_{inj} = 5$ and 12

For the purpose of investigating the influence of the disintegration on the jet dynamics, the axial and radial Reynolds stresses are analyzed for both cases. To understand the Reynolds stress distribution at the shear layer between cold and warm nitrogen, the radial position of the maximum values located at the position of jet surface $r/D_{inj} = 0.5$ are used to evaluate their evolution. Figure 7 shows the axial and radial Reynolds stress as function of injector distance for both the transcritical and supercritical cases. In both cases, the axial fluctuation starts with a small growth along with sharply increase until achieving a relative stable state at around $x/D_{inj} = 5$ for Case 2, while $x/D_{inj} = 10$ for Case 1. Note that the axial fluctuations reach significantly higher values in the transcritical case. However, different from the axial fluctuation, the radial fluctuations show zero growth near the injector before $x/D_{inj} = 3$ and 1.5 for the transcritical and supercritical cases, respectively. After that the fluctuations begin to grow and the growth rate is much higher in the supercritical case and the fluctuation reach significantly larger values for the supercritical case. This can be due to the density stratification effect, which is stronger in the transcritical case, suppressing the velocity fluctuation and turbulent movement to radial direction.

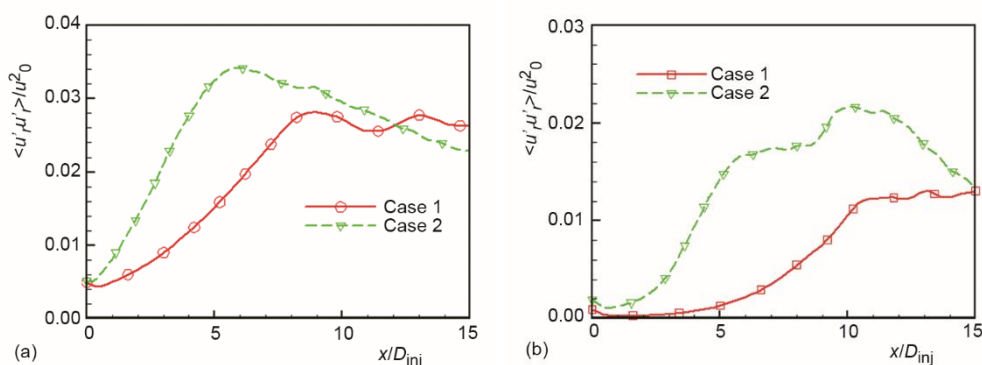


Figure 7. The axial (a) and radial (b) Reynolds stresses as function of injector distance

Figure 8 shows the radial profiles of Reynolds stresses that further illustrate the influence of the disintegration characteristic on mixing behavior. At $x/D_{inj} = 3$, which is much close to the injector, a narrow peak values exist in the jet surface, while the peaks are broader and has a much larger value for the supercritical case. The radial fluctuations are clearly influenced by the density gradient, where the Reynolds stresses in the transcritical case are significantly suppressed due to its large density stratification. On the contrary, the radial fluctuation in the supercritical is much stronger and spread deep into the radial direction. In addition, one can notice that the peaks shift to higher values of r/D_{inj} , while the peaks are suppressed and become flat due to the jet disintegration characteristics. This disintegration mechanism is delayed for the transcritical injection, because the jet surface is stabilized by higher density gradient (shown in fig. 4) and surrounded by a high specific heat (shown in fig. 6) effects. As the jet develop downstream at $x/D_{inj} = 5, 8,$ and 10 , the disintegration mechanism is more obvious, so that the peaks in both cases move deeper into the radial direction and the peaks become broader with the increase of the values of x/D_{inj} . By close inspection, it can be found that the radial fluctuations are stronger as the jet move downstream, while the axial fluctuations show different profiles. Initially, the axial fluctuation in the supercritical increase as the jet move to $x/D_{inj} = 5$, while decrease at $x/D_{inj} = 8$ and 10 . However, the fluctuations in the

transcritical case continuously grow until $x/D_{inj} = 10$. This phenomenon can be explained by the disintegration mechanism, where the large density stratification has the effects of stabilizing the jet flow, delaying the disintegration in the transcritical case.

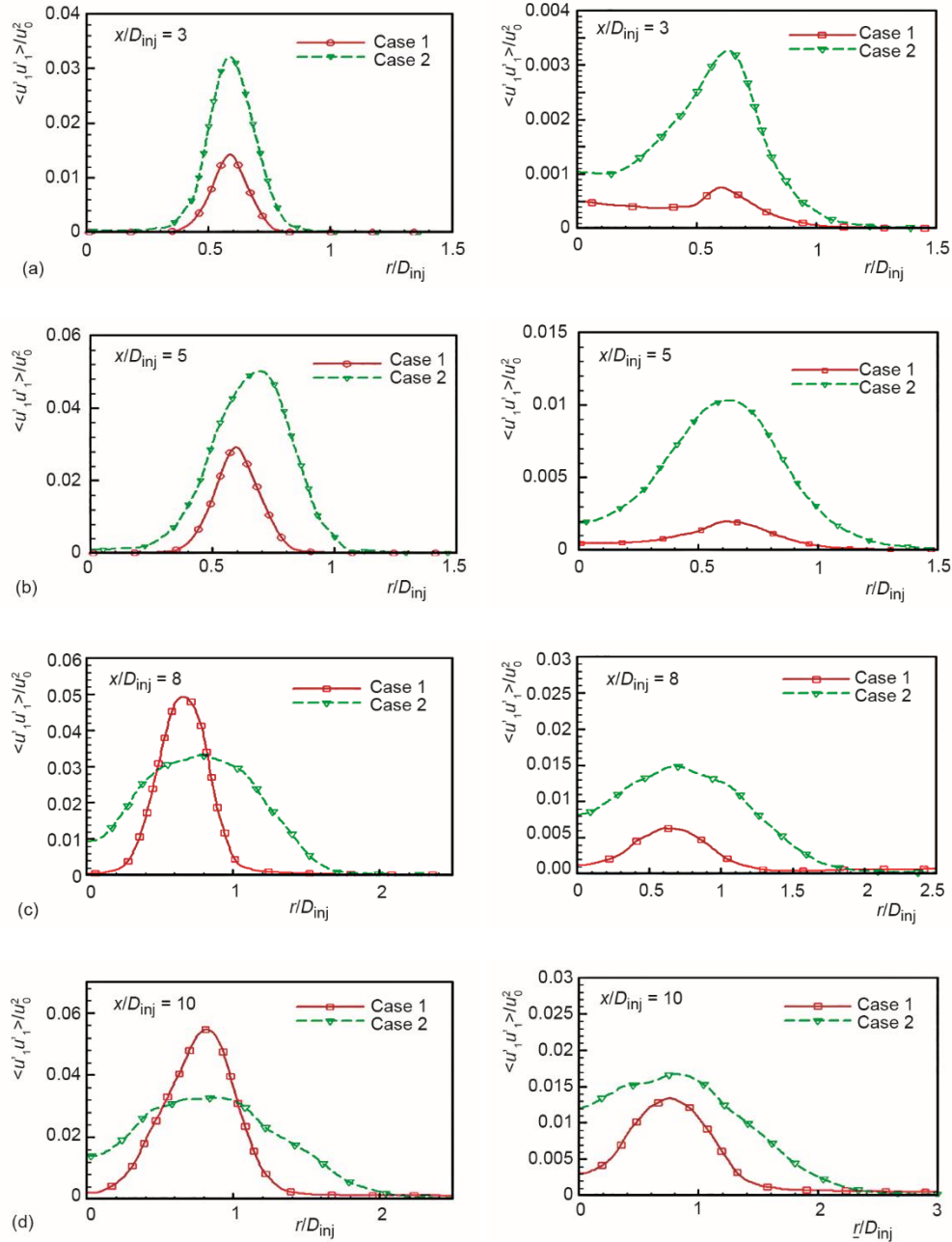


Figure 8. The axial and radial Reynolds stresses as function of the radial distance from the centerline at injector distances $x/D_{inj} = 3, 5, 8,$ and 10

As mentioned in previous analysis, the jet disintegration characteristics present a significant importance to the velocity fluctuation and jet mixing behavior. Hence, in this study, we focus on presenting a new interpretation of jet disintegration to further understand the disintegration mechanism in both transcritical and supercritical conditions. The jet field can be divided into four parts: the length of liquid-like core L_L at $T - T_c < 0$, the length of the dense core L_D that the density-gradient reach to a maximal value, the end of the transitional region L_T where the density-gradient come to an unchanged region, and after the end of the transitional region L_T , the jet will reach a self-similar state, L_S .

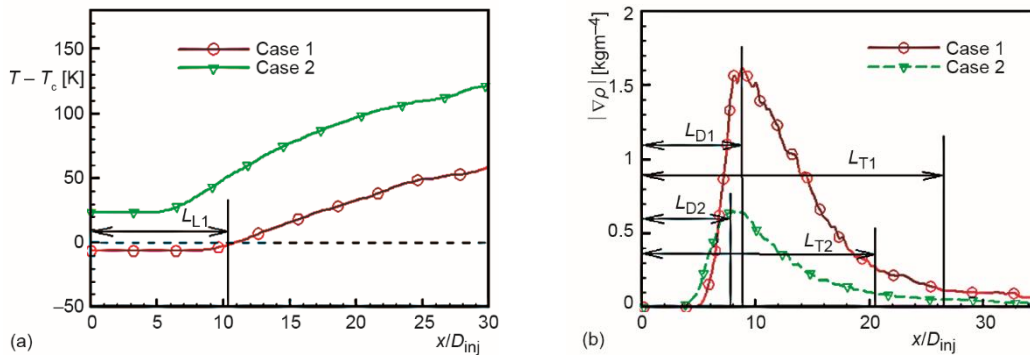


Figure 9. The $T - T_c$ distribution (a) and density-gradient (b) along the jet centerline

According to the definition, fig. 9 shows the $T - T_c$ distribution and density-gradient along the jet centerline and each division parts are also marked on the figure, whose length are summed up in tab. 4. One can notice that the liquid nitrogen is still exists and move far downstream at about $x/D_{inj} = 10.1$ in the transcritical case, hence the jet must transit across the pseudo critical temperature and more energy is needed to expand its volume, rather than to increase the temperature. The existence of the liquid core indicates that the surface tension may not disappear completely. However, in the supercritical case, the liquid nitrogen is invisible, implying that the intensive turbulent diffusion dominates the mixing process. Because of this reason, the fluctuation is much stronger in the supercritical case. In addition, the length of the dense core, L_D , and the end of transition region, L_T , show higher value in the transcritical injection than in the supercritical injection, which can be explained by two reasons. First, the initial injection temperature is below the critical temperature ($T_c = 126.3$ K), leading to a larger density stratification in the transcritical case, second, the transcritical case transit across the pseudo critical temperature that much more heat is absorbed to expand its volume. Therefore, much larger density gradients are formed around the jet surface, which transfer the turbulence kinetic energy from the radial to the axial direction. The different disintegration process demonstrate that the supercritical jet tends to be more easily mixed with the ambient gas, so that the flow can be more earlier come to the self-similar region.

Table 4. The length of disintegration at each part for the transcritical and supercritical injection

Length type	Case 1/ D_{inj}	Case 2/ D_{inj}
L_L	10.2	—
L_D	8.90	7.90
L_T	26.5	20.4

In the latest investigation, Dahms *et al.* [36] devoted to performing an investigation in what pressure and temperature conditions the interface structure transition to dense-fluid mixing dynamics occurs. The results were based on micro-scale flows and indicated that the mixing layer characteristics are depended on the initial injection and chamber conditions. To further understand the mixing layer interface in macro-scale fluids, the mixing layer thickness based on the density gradients are analyzed to reveal the mixing feature on both transcritical and supercritical injection. Figure 10 shows the radial distributions of density gradient in two axial positions at $x/D_{inj} = 4$ and 9 for both cases. Close to the injector region at $x/D_{inj} = 4$, the transcritical case shows a much higher value and reach a maximum value at the jet surface for both cases. As the jet move downstream ($x/D_{inj} = 9$), the values decrease and the maximum values tend to move to the axial position. One can notice that the density gradient values are much larger in the transcritical injection, which is consistent with the contour plots in fig. 4. To reveal the jet-gas interface properties, we define a mixing layer thickness, d , which is the distance from the maximum density gradient $|\nabla\rho|_{max}$ to the point where this value drops to $0.1|\nabla\rho|_{max}$ along the radial direction. According to the definition, the mixing layer thickness is also marked in fig. 10, where d_1 and d_2 represent the transcritical and supercritical injection, respectively. In addition, the values of the mixing layer thickness are listed in tab. 5. It can be observed that both cases show a much larger value in the regions of $x/D_{inj} = 9$ than that in $x/D_{inj} = 4$ and the ratio of their values are about 4. By comparing the two cases, it can be found that the supercritical case has a larger value with a ratio of their values are about 1.4 at $x/D_{inj} = 4$ and $x/D_{inj} = 9$. These results indicate that the initial injection temperature in the transcritical case is below its critical temperature and the density stratification is larger, resulting in a much larger density gradient across the jet interface, which has the effects of stabilizing the fluid flow. As a result, a thinner mixing layer interface is formed and is unhelpful to the mixing of the jet and surrounding gas. In addition, the disintegration process is delayed due to the thinner mixing layer interface in the transcritical case, so that a longer potential core is formed, which can be found in fig. 9.

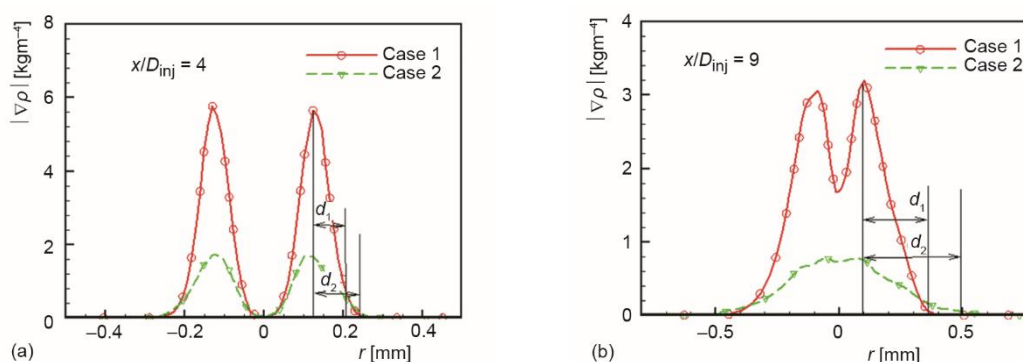


Figure 10. Density gradient in radial distribution at (a) $x = 4$ mm and (b) $x = 9$ mm for both cases

Table 5. Mixing layer thickness based on the density gradient

Position/ D_{inj}	Case 1	Case 2
$x = 4$	0.071 mm	0.101 mm
$x = 9$	0.280 mm	0.403 mm

Conclusions

In the present study, the mixing behavior of transcritical and supercritical injections of nitrogen are studied by large eddy simulation. The PISO algorithm is modified to handle real fluid state due to the thermodynamic non-ideality and anomalies in transport properties under supercritical conditions. The instantaneous flow field and mean quantities are analyzed to reveal the different mixing feature between the transcritical and supercritical injection.

The density gradient is of significant importance to the mixing of the injected fuels and surrounding gas and the transcritical injection shows much larger values. These large density gradients suppress the development of the instability waves and the jet fluid tends to develop downstream. As a result, the jet disintegration is delayed and longer dense core region is detected. In addition, *liquid* block can be seen in the transcritical case, while this phenomenon does not occur in the supercritical jet. Besides, large specific heat and transport properties tend to locate on the large density gradient regions, it is obviously that the large density gradients are influenced by the pseudo critical temperature and transport properties.

In order to understand the disintegration characteristics, we define the disintegration length for both the transcritical and supercritical cases. According to our definition, *liquid nitrogen* is still exists while this is invisible in the supercritical injection, and a longer dense core is found in the transcritical case and the jet will move further downstream before reaching a self-similar region. Because of this disintegration mechanism, the Reynolds stresses in the transcritical case are significantly suppressed in the turbulent fluctuation, where the turbulent diffusion dominates the mixing process.

Base on the density gradient, the jet-gas interface properties are analyzed to reveal the mixing behavior. To quantify the jet-gas interface and mixing layer characteristics, we define a mixing layer thickness based on the density gradient. Results indicate that in the supercritical injection, the mixing layer shows much larger thickness, which is helpful to the mixing of the jet and surrounding gas. In addition, an earlier disintegration characteristic is visible due to the thicker mixing layer interface in the supercritical case. The results obtained in this study provide some insight into the differences between transcritical and supercritical injection.

Acknowledgment

This work is supported by National Natural Science Foundation of China (Grant No. 52066004, No.51576029), Guizhou Science and Technology Plan Project (Grant No. [2020]1Y237). Guizhou University introduces talent research (Grant No.(2018)19).

Nomenclature

e_t – total energy
 H_i^{SGS} – sub-grid scale energy fluxes
 L_D – dense core
 L_S – self-similar state
 L_T – transitional region
 p – pressure
 P_c – critical pressure
 S_{ij}^{SGS} – sub-grid scale strain-rate tensor
 T – temperature
 T_∞ – environment temperature
 T_c – critical temperature
 T_{inj} – inject temperature

Greek symbols

ρ_c – critical density
 ρ_{inj} – inject density
 ρ_∞ – environment density
 τ_{ij} – sheer stress
 σ_{ij} – viscous work

Acronyms

SRK – Soave-Redlich-Kwong
LES – large eddy simulation
FWHM – full width, half maximum
HWHM – half width, half maximum

References

- [1] Chehroudi, B., et al., Cryogenic Shear Layers: Experiments and Phenomenological Modeling of the Initial Growth Rate Under Subcritical and Supercritical Conditions, *International Journal of Heat & Fluid Flow*, 23 (2002), 5, pp. 554-563
- [2] Chehroudi, B., et al., Visual Characteristics and Initial Growth Rates of Round Cryogenic Jets at Subcritical and Supercritical Pressures, *Physics of Fluids*, 14 (2002), 2, pp. 850-861
- [3] Mayer, W., et al., Raman Measurements of Cryogenic Injection at Supercritical Pressure, *Heat & Mass Transfer*, 39 (2003), 8-9, pp. 709-719
- [4] Oschwald, M., Schik, A., Supercritical Nitrogen Free Jet Investigated by Spontaneous Raman Scattering, *Experiments in Fluids*, 27 (1999), 6, pp. 497-506
- [5] Davis, D. W., Chehroudi, B., Measurements in an Acoustically Driven Coaxial Jet under Sub-, Near-, and Supercritical Conditions, *Journal of Propulsion & Power*, 23 (2007), 2, pp. 364-374
- [6] Miller, R. S., et al., Direct Numerical Simulations of Supercritical Fluid Mixing Layers Applied to Heptane-Nitrogen, *Journal of Fluid Mechanics*, 436 (2001), 4, pp. 1-39
- [7] Okong'O, N. A., Bellan, J., Direct Numerical Simulation of a Transitional Supercritical Binary Mixing Layer: Heptane and Nitrogen, *Journal of Fluid Mechanics*, 464 (2002), 10, pp. 1-34
- [8] Taskinoglu, E. S., Bellan, J., A Posteriori Study Using a DNS Database Describing Fluid Disintegration and Binary-Species Mixing Under Supercritical Pressure: Heptane and Nitrogen, *Journal of Fluid Mechanics*, 645 (2010), 3, pp. 211-254
- [9] Selle, L., Schmitt, T., Large-Eddy Simulation of Single-Species Flows Under Supercritical Thermodynamic Conditions, *Combustion Science and Technology*, 182 (2010), 4-6, pp. 392-404
- [10] Yang, N. Z., Vigor, An Efficient Preconditioning Scheme for Real-Fluid Mixtures Using Primitive Pressure-Temperature Variables, *International Journal of Computational Fluid Dynamics*, 21 (2007), 5, pp. 217-230
- [11] Zong, N., et al., A Numerical Study of Cryogenic Fluid Injection and Mixing Under Supercritical Conditions, *Physics of Fluids*, 16 (2004), 12, pp. 4248-4261
- [12] Park, T. S., LES and RANS Simulations of Cryogenic Liquid Nitrogen Jets, *Journal of Supercritical Fluids*, 72 (2012), 12, pp. 232-247
- [13] Simeoni, G. G., The Widom Line as Crossover Between Liquid-Like and Gas-Like Behaviour in Supercritical Fluids, *Nature Physics*, 6 (2010), 7, pp. 503-507
- [14] Banuti, D. T., Crossing the Widom-Line – Supercritical Pseudo-Boiling, *Journal of Supercritical Fluids*, 98 (2015), Mar., pp. 12-16
- [15] Banuti, D. T., Hannemann, K., The Absence of a Dense Potential Core in Supercritical Injection: A Thermal Break-Up Mechanism, *Physics of Fluids*, 28 (2016), 3, 035103
- [16] Sarkar, J., Improving Thermal Performance of Microchannel Electronic Heat Sink Using Supercritical CO₂ as Coolant, *Thermal Science*, 23 (2017), 1, pp. 30-30
- [17] Bai, W., Xu, X., Comparative Analyses of Two Improved CO₂ CCHP Systems Driven by Solar Energy, *Thermal Science*, 22 (2018), Suppl. 2, pp. S54-S54
- [18] Branam, R., Mayer, W., Characterization of Cryogenic Injection at Supercritical Pressure, *Journal of Propulsion & Power*, 19 (2003), 3, pp. 342-355
- [19] Zong, N., Yang, V., Cryogenic Fluid Jets and Mixing Layers in Transcritical and Supercritical Environments, *Combustion Science & Technology*, 178 (2006), 1, pp. 193-227
- [20] Yue, H. Y., Liu, Z. G., Viscosity Prediction of Refrigerants Under Subcritical/Supercritical Conditions, *Thermal Science*, 19 (2015), 4, pp. 1293-1296
- [21] Benarous, A., Liazid, A., H-2-O-2 Supercritical Combustion Modeling Using a CFD Code, *Thermal Science*, 13 (2009), 3, pp. 139-152
- [22] Wang, X., et al., Numerical Study on Nonuniform Heat Transfer of Supercritical Pressure Carbon Dioxide During Cooling in Horizontal Circular Tube, *Applied Thermal Engineering*, 141 (2018), Aug., pp. 775-787
- [23] Fang, T. H., et al., Effects of Temperature and Aperture Size on Nanojet Ejection Process by Molecular Dynamics Simulation, *Microelectronics Journal*, 35 (2004), 9, pp. 687-691
- [24] Smagorinsky, J., General Circulation Experiments with The Primitive Equations, *Monthly Weather Review*, 91 (1963), 3, pp. 99-164

- [25] Jacobsen, R. T., Stewart, R. B., Thermodynamic Properties of Nitrogen Including Liquid and Vapor Phases from 63 K to 2000 K with Pressures to 10,000 Bar, *Journal of Physical & Chemical Reference Data*, 2 (2009), 4, pp. 757-922
- [26] Prausnitz, M., *Molecular Thermodynamics of Fluid-Phase Equilibria*, Prentice-Hall, Upper Saddle, River, N. J., USA, 1969
- [27] Graboski, M. S., Daubert, T. E., A Modified Soave Equation of State for Phase Equilibrium Calculations. 1. Hydrocarbon Systems, *Journal of Alloys & Compounds*, 19 (1980), 3, pp. 429-435
- [28] Soave, G., Equilibrium Constants from a Modified Redlich-Kwong Equation of State, *Chemical Engineering Science*, 27 (1972), 6, pp. 1197-1203
- [29] Kim, S. K., et al., Thermodynamic Modeling Based on a Generalized Cubic Equation of State for Kerosene/LOx Rocket Combustion, *Combustion & Flame*, 159 (2012), 3, pp. 1351-1365
- [30] Zeberg-Mikkelsen, C. K., Stenby, E. H., Viscosity Modeling of Light Gases at Supercritical Conditions Using the Friction Theory, *Industrial & Engineering Chemistry Research*, 40 (2001), 17, pp. 3848-3854
- [31] Vasserman, A. A., Nedostup, V. I., An Equation for Calculation of the Thermal Conductivity of Gases and Liquids, *Journal of Engineering Physics*, 20 (1971), 1, pp. 89-92
- [32] ***, <http://webbook.nist.gov/chemistry/fluid>
- [33] Park, T. S., Effects of Time-Integration Method in a Large-Eddy Simulation Using the PISO Algorithm: Part I-Flow Field, *Numerical Heat Transfer, Part A: Applications*, 50 (2006), 3, pp. 229-245
- [34] Kim, S. K., Park, T. S., A Pressure-Based Algorithm for Gaseous Hydrogen/Liquid Oxygen Jet Flame at Supercritical Pressure, *Numerical Heat Transfer, Part A: Applications*, 67 (2015), 5, pp. 547-570
- [35] Mathey, F., et al., Specification of LES Inlet Boundary Condition Using Vortex Method, *Progress in Computational Fluid Dynamics, Inderscience*, 6 (2006), pp. 58-67
- [36] Dahms, R. N., Oefelein, J. C., Non-Equilibrium Gas-Liquid Interface Dynamics in High-Pressure Liquid Injection Systems, *Proceedings of the Combustion Institute*, 35 (2013), 2, pp. 1587-1594